WEP Warwick Evans Publishing

Academic Journal of Management Science and Engineering

ISSN: 3080-9827 (Print), ISSN: 3080-9835 (Online) | Volume 1, Number 2, Year 2026
DOI: https://doi.org/10.62051/ajmse.v1n2.10
Journal homepage: https://ajomse.com



Study on the Bonding Performance and Reinforcement Mechanism of the Second Interface of Cement Sheath

Chongyang Liu

School of Pipeline Engineering, Xi'an Shiyou University, Xi'an, Shaanxi, China

ABSTRACT

To address the engineering challenge of debonding failure of the "second interface" (between the cement sheath and the formation rock) induced by alternating thermal-mechanical loads during geothermal well cementing, this study systematically investigated the reinforcement mechanism of a hybrid system of graphene and carbon nanotubes (CNTs) on the second-interface bonding performance of cement stone, using typical sandstone cores from the Ordos Basin as the substrate. The evolution of interfacial bond strength and failure mode under different CNTs contents (0%–0.12%) was evaluated by push-out shear tests. Combined with microstructural characterization techniques such as FE-SEM and EDS, the densification and toughening mechanisms of the interfacial transition zone (ITZ) were revealed from the perspectives of morphological evolution, element migration, and chemical bonding. The results showed that the 28-day second-interface bond strength reached 8.20 MPa, representing an approximately 15-fold increase compared to the baseline group (0.51 MPa). The shear stress–slip curve transitioned from a brittle "cliff-like" drop to a "pseudo-ductile" failure with serrated rebounds, indicating significantly enhanced fracture toughness. Microstructural analysis confirmed that graphene provided "template nucleation" and a two-dimensional skeleton, while CNTs played a "bridging–pull-out" energy dissipation role spanning cracks. Together, they constructed a "line-surface" three-dimensional interpenetrating network, reducing the interfacial Ca/Si atomic ratio from 0.59 to 0.43 and driving the interface bonding from physical van der Waals forces to chemical covalent bonds (Si–O–Si/Si–O–Ca). Excessive CNTs (≥0.12%) led to agglomeration, forming stress concentration sites and causing a decline in strength. This study provides a theoretical basis and material proportioning reference for the integrated design of "high thermal conductivity" and "strong interface" in geothermal well cementing.

KEYWORDS

Geothermal Cementing; Second Interface; Carbon Nanotubes (CNTs); Bond Strength; Pseudo-ductile Failure; Interfacial Transition Zone (ITZ); Chemical Bonding.

1. INTRODUCTION

As a critical barrier for sealing formations, supporting casings, and establishing heat transfer pathways, the cement sheath's bulk property enhancement alone is insufficient to ensure long-term production safety for deep and complex geothermal reservoirs such as those in the Ordos Basin [1-3] The bonding strength and sealing durability of the cementing interface, particularly the second interface between the cement sheath and the formation rock, constitute the "lifeline" for ensuring the century-long wellbore integrity of geothermal wells [4-6].

During alternating operations of long-term heat extraction and cold fluid injection, geothermal wells experience frequent and severe temperature fluctuations [7-8]. This long-term thermal cycling generates significant alternating thermal stresses due to the inherent differences in thermal expansion coefficients among the casing, cement sheath, and formation. These stresses readily induce bulk

Content from this work may be used under the terms of CC BY-NC 4.0 licence (https://creativecommons.org/licenses/by-nc/4.0/).
Published by Warwick Evans Publishing.

damage to the cement sheath and fatigue debonding at the interface, thereby creating micro-annuli that can lead to fluid channeling[9-11]. Furthermore, the second interface system involves complex interactions among the formation rock, drilling fluid filter cake, and cement stone, and is regarded as the most vulnerable sealing node in the entire cementing defense line [12-15]. Current research on interfacial bond strength largely remains at the level of obtaining macroscopic mechanical parameters, with insufficient exploration of active reinforcement methods for the complex interfacial transition zone (ITZ) at the nanoscale. Notably, there is a significant knowledge gap regarding how carbon nanomaterials fundamentally reconstruct the interface microstructure from physical and chemical perspectives [16-17].

To address this, the research perspective of this chapter extends from the cement "bulk" to the "second interface", aiming to systematically reveal the strengthening effect of the hybrid nanomaterial system on second-interface bonding performance[18-19]. Field cores of typical sandstone reservoirs from the Ordos Basin were selected as the substrate to realistically replicate the "rock-cement stone" composite interface [20]. A novel push-out shear test was designed to quantitatively evaluate the bonding and slip failure behavior of the interface under alternating thermal-mechanical conditions. On this basis, field-emission scanning electron microscopy (FE-SEM) and energy-dispersive X-ray spectroscopy (EDS) mapping were comprehensively employed to directly analyze the topological morphology evolution, hydration product attachment, and cross-interface element migration patterns of the ITZ at the nanoscale. This chapter aims to clarify the synergistic contributions of CNTs ("crack-bridging anchoring") and graphene ("surface nucleation chemical optimization") in preventing second-interface debonding through cross-scale mechanical and chemical experiments, thereby providing critical theoretical and data support for the integrated engineering design of "high thermal conductivity" and "strong interface" in geothermal cementing.

2. EXPERIMENTAL DESIGN

2.1. Specimen Preparation

The sandstone core specimens used in this study were taken in situ from an outcrop of a geothermal reservoir in the Ordos Basin (Figure 1). Through coring and subsequent processing, standard cylindrical specimens with dimensions of Φ25 mm × 40 mm were prepared. The machining accuracy of the cores was strictly controlled according to the ISRM suggested methods [108] and the Chinese standard GB/T 50266-2013, ensuring that the final specimens met the following geometric tolerance requirements: non-parallelism of the end faces less than 0.05 mm, diameter deviation not greater than 3 mm, and perpendicularity deviation between the end face and axis less than 0.25°.

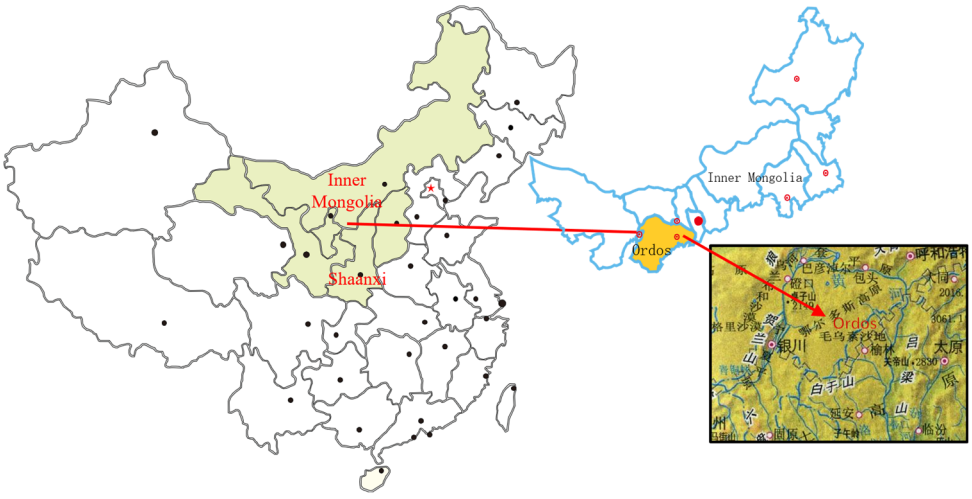


Figure 1. Geographical location of the core

The specific preparation procedure for the “rock-cement” composite bonded specimens in this study is illustrated in Figure 2. The steps were as follows. First, a standard sandstone core was placed in the center of a cylindrical mold (Φ50 mm × 32 mm). To prevent bottom adhesion and reserve space for subsequent push-out testing, a silicone gasket with a thickness of 4.15 mm was placed between the bottom of the core and the mold base, creating an axial gap. Subsequently, the uniformly mixed nanocomposite cement slurry was slowly injected along the inner wall of the mold using the edge-pouring method, allowing it to fill the annular space between the core and the mold under its own weight. After casting, gentle vibration was applied to remove residual air bubbles, and the upper surface was leveled. Finally, the mold surface was sealed with plastic wrap, and the specimen was placed in a constant-temperature water bath for curing for 72 hours. During curing, the water level was strictly controlled to just cover the bonded interface between the rock and the cement stone without exceeding the top of the mold. After curing, the specimen was demolded, yielding the desired second-interface bonded specimen.

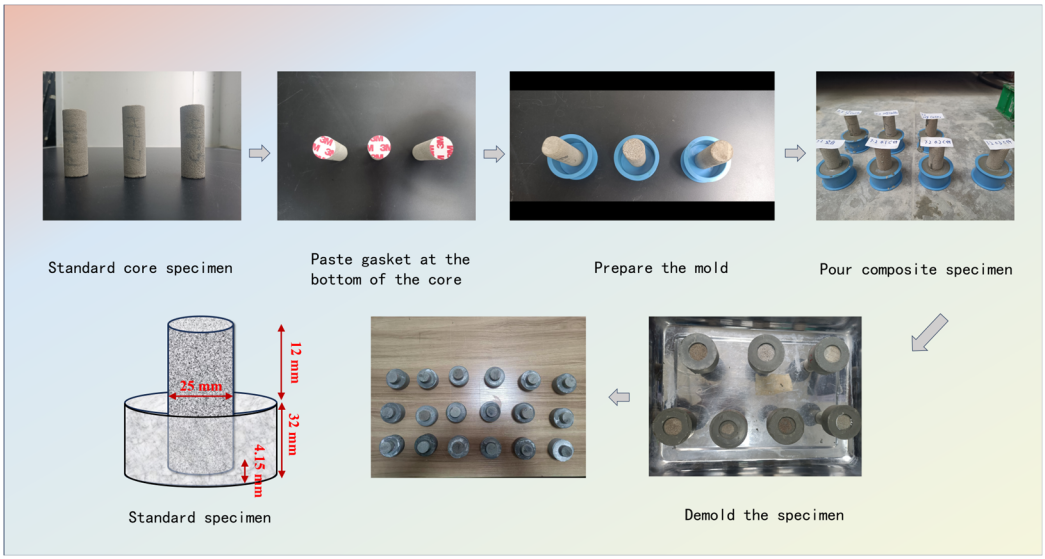


Figure 2. Preparation process of bonded specimens

2.2. Mix Proportion Design of Second-Interface Bonded Specimens

Table 1. Mix proportions of cement (wt.%)

No	Cement	w/c	Graphene (%)	CNTs(%)	Quartz powder	Silica fume	Water reducer	Fluid loss reducer	Defoamer
B0	1	0.44	0.00	0	0.6	0.05	0.6	0.5	0.2
C0	1	0.44	0.10	0	0.6	0.05	0.6	0.5	0.2
C1	1	0.44	0.10	0.02	0.6	0.05	0.6	0.5	0.2
C2	1	0.44	0.10	0.04	0.6	0.05	0.6	0.5	0.2
C3	1	0.44	0.10	0.06	0.6	0.05	0.6	0.5	0.2
C4	1	0.44	0.10	0.08	0.6	0.05	0.6	0.5	0.2
C5	1	0.44	0.10	0.10	0.6	0.05	0.6	0.5	0.2
C6	1	0.44	0.10	0.12	0.6	0.05	0.6	0.5	0.2

the water-to-cement ratio was fixed at 0.44, and the base components consisted of Class G oil well cement, 5% quartz powder, and 60% silica fume. With the graphene content maintained at 0.10%, the CNTs content was varied in a continuous gradient from 0% to 0.12% at intervals of 0.02% (a total of seven levels). Additionally, a plain baseline group without any nanomaterials (B0) and a control group containing only 0.10% graphene (C0) were established to precisely quantify and isolate the absolute contribution of CNTs incorporation to the second-interface bond strength. The detailed mix proportions are presented in Table 1.

2.3. Second-Interface Testing Methods

(1) Interface Push-Out Shear Test: A standard gantry-type WDW microcomputer-controlled electronic universal testing machine was used for this test, which is primarily designed for mechanical property testing and analysis of various metals, non-metals, and composite materials. The machine has a maximum test force of 100 kN, a test force accuracy of ±0.5% of the indicated value, a deformation measurement range of 2%–100% FS, a deformation resolution of 0.01 mm (with an optional extended range of 10–500 mm), and a displacement indication error of ±0.5% of the indicated value. Three control modes (load, displacement, and deformation) are available, with random switching among them. The system can simultaneously plot various test curves, such as force-elongation, stress-strain, force-time, and stress-time curves, as well as a test force-displacement curve.

The data acquisition system employed an AD800 data acquisition card, which can be inserted directly into any PCI slot of the computer, simplifying the circuit structure, accelerating the sampling rate, and improving the accuracy and stability of the measurement and control system. The displacement measurement device of the testing machine uses a 2000-line photoelectric encoder, with a relative accuracy of up to ±0.5%.

The “push-out method” (Figure 3) was adopted for testing. During the test, an axial load was applied to the central core by the testing machine at a constant displacement rate. The data acquisition system simultaneously recorded the load-displacement curve. The maximum peak load (F) required to completely strip and push the core out of the cement sheath was recorded, allowing quantitative evaluation of the interfacial bonding quality. A higher second-interface bond strength between the core and the cement stone indicates superior interfacial bonding performance. The specific calculation formula is as follows:

$$P=\frac{F}{S} \tag{1}$$

where "P" is the interfacial bond strength between the core and the cement stone (MPa),F is the maximum force required to push the core out of the cement sheath (kN),and S is the bonded area between the core and the cement stone (cm^2)

(2) Interfacial Microstructure and Element Migration Tracking: To deeply reveal the micro-reinforcement mechanism of CNTs on the second-interface bond strength between sandstone and cement stone from the Ordos Basin, macroscopic mechanical testing was linked with microstructural evolution. Microscopic characterization of the ITZ at the second interface was performed. Given the extremely small and complex structure of the second-interface region, conventional bulk analysis methods (such as XRD and TGA) cannot accurately isolate interfacial information. Therefore, SEM and EDS were used as the core characterization techniques. The specific test method and sample preparation process are shown in Figure 4.

Interfacial Micro-Specimen Preparation: Typical interface-containing fragments after failure in the macroscopic push-out test were taken, or the uncured bonded specimens were cut axially to obtain miniature thin sections (approximately 10 mm × 10 mm × 5 mm) containing the complete “rock-interface-cement stone” transition zone. The cut specimens were immersed in anhydrous ethanol for 24 hours to stop hydration, then dried in a 50 °C vacuum oven to constant weight. To obtain clear

interfacial observation and eliminate charging effects, the observation surface was finely mechanically polished and coated with gold by ion sputtering.

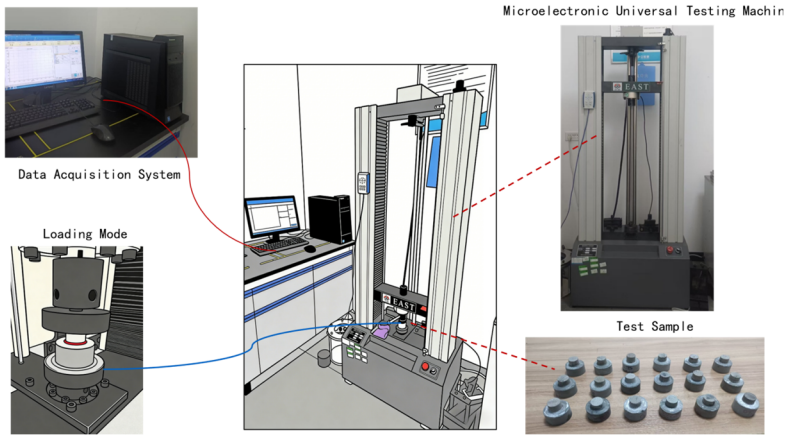


Figure 3. Schematic diagram of the interfacial bond strength test

SEM: The prepared specimens were placed in the specimen chamber of a field-emission scanning electron microscope. The junction region between the sandstone and the composite cement stone was focused on, observing the width variation of the ITZ, the initiation and propagation morphology of microcracks, and the attachment and crystallization state of hydration products (such as C-S-H gel and AFt) on the rock surface. In particular, at high magnification, the spatial distribution characteristics of CNTs at the interface were sought and recorded, obtaining direct visual evidence of CNTs spanning microcracks and playing a “bridging anchoring” and “reinforcing” role.

EDS: Simultaneously with SEM morphology observation, EDS line scans and point scans were performed across the interface region. By quantitatively tracking the concentration gradient distribution of characteristic elements (such as Ca, Si, and Al) from the cement matrix through the ITZ to the interior of the sandstone, the in-depth influence of nanomaterial incorporation on interfacial chemical bonding and the enrichment state of hydration products was evaluated.

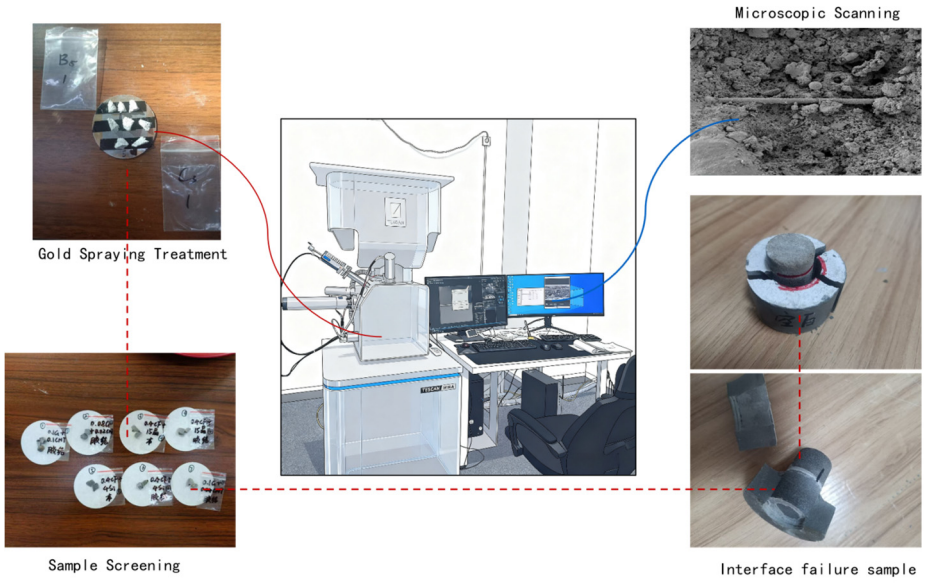


Figure 4. Schematic diagram of interfacial microstructure scanning

3. ANALYSIS OF SECOND-INTERFACE BOND STRENGTH AND FAILURE CHARACTERISTICS

3.1. Evolution Law of Second-Interface Bond Strength

To quantitatively evaluate the influence of carbon nanotube (CNTs) content on the second-interface bonding quality of cementing, push-out tests were performed on bonded specimens with different mix proportions at curing ages of 7 days and 28 days. Figure 5 intuitively shows the evolution of the second-interface bond strength for each group. Overall, the combined incorporation of graphene and CNTs significantly enhanced the interfacial bonding performance, exhibiting a typical "rapid growth—saturation—agglomeration-induced decay" pattern for nanocomposites. Moreover, the composite system demonstrated superior long-term interface strengthening capability. The detailed analysis can be divided into the following four evolution stages and the long-term strengthening mechanism.

Basic Strengthening Stage (B0 to C0): The plain cement baseline group (B0) exhibited extremely low second-interface bond strength, only 0.41 MPa at 7 days and 0.51 MPa at 28 days. This was due to the bleeding and shrinkage of conventional cement slurry in the early hydration stage, as well as the weak adhesion of hydration products to the rock surface, resulting in significant structural defects in the ITZ. With the addition of 0.10% graphene alone (Group C0), the 7-day strength jumped to 2.11 MPa, and the 28-day strength reached 2.68 MPa. Owing to its large specific surface area, two-dimensional flake-like graphene acted as an excellent nucleation site on the rock surface, promoting the oriented growth of dense hydration products, filling micron-scale pores, and preliminarily improving the mechanical interlocking between the cement stone and the sandstone.

Rapid Synergistic Growth Stage (C0 to C2): Upon introducing a small amount of CNTs (0.02%–0.04%) into the 0.10% graphene network, the interfacial strength experienced explosive growth. The 7-day and 28-day strengths of Group C2 (0.04% CNTs) surged to 5.88 MPa and 7.64 MPa, respectively. At this stage, the one-dimensional fibrous CNTs interspersed between the two-dimensional graphene sheets began to exert a significant cross-scale "bridging" effect. When subjected to interfacial shear stress, the uniformly dispersed CNTs acted like "micro-rebars" spanning interface microcracks, bearing part of the shear stress. Through their own tensile deformation and pull-out energy dissipation, they greatly enhanced the fracture toughness of the ITZ, leading to a transition of bond failure from brittle to a certain degree of ductility.

Peak Saturation Stage (C3 to C5): As the CNTs content continued to increase from 0.06% to 0.10%, the absolute value of the interfacial strength continued to increase, but the growth rate slowed significantly. At Group C5 (0.10% CNTs), the interfacial bond strength reached its global maximum: 6.06 MPa at 7 days and 8.20 MPa at 28 days. At this point, the "line-surface" three-dimensional spatial network constructed by graphene and CNTs within the matrix and at the interface achieved optimal packing density. A large number of CNTs achieved multiple bridging of microcracks, and the mechanical transmission efficiency of the network skeleton reached its peak. It is worth noting that this optimal proportion for second-interface strength (0.10% graphene + 0.10% CNTs) is completely consistent with the optimal proportions for bulk thermal conductivity and compressive strength found in Chapter 3, confirming the high compatibility of this nanocomposite system in achieving the dual functions of "high thermal conductivity" and "strong interface".

Agglomeration Decay Stage (C6): When the CNTs content further exceeded the threshold to 0.12% (Group C6), the interfacial strength decreased significantly (7-day strength dropped to 5.42 MPa, 28-day strength to 6.18 MPa). Due to the enormous van der Waals forces and high surface energy of the excess nanotubes, which exceeded the suspension limit of the dispersant, severe entanglement and agglomeration of CNTs occurred in the cement slurry. These macro-scale agglomerates not only lost their "bridging" capability across cracks but also became low-strength "weak inclusions" within the interface-sensitive zone. They hindered the normal hydration of cement particles and introduced

additional structural pores and stress concentration points, resulting in a sharp reduction in the effective physical bonding area at the interface.

Comparing the data for each group, it is clear that the 28-day interfacial strength of all specimens was higher than their 7-day strength. The long-term increase was particularly significant for the composite groups (C1–C5) (the strength of Group C5 increased by approximately 35%). This long-term strengthening is mainly attributed to chemical filling effects and physical shrinkage resistance.

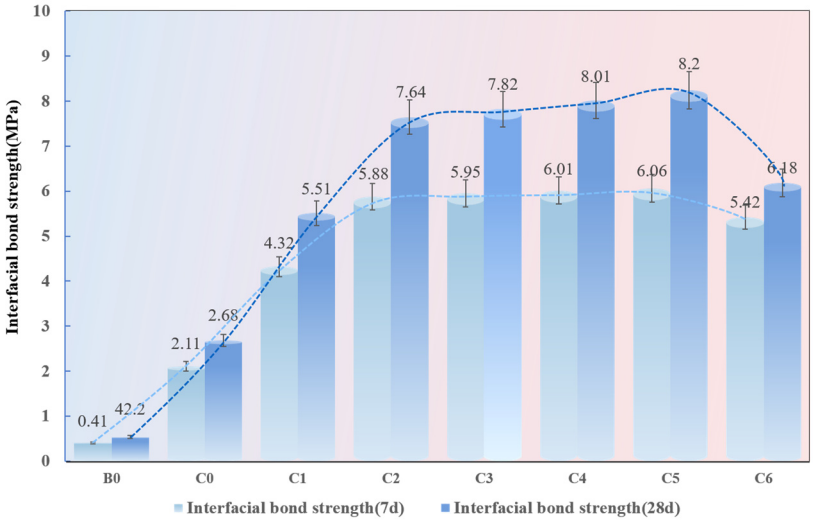


Figure 5. Trend of second-interface bond strength

3.2. Analysis of Second-Interface Failure Mode and Toughening Mechanism

The failure of the second interface depends not only on the ultimate bond strength but also on the ductility, fracture toughness, and residual friction during the failure process. These factors are equally critical for resisting complex thermal-mechanical alternating loads in geothermal wells and ensuring long-term wellbore sealing. By analyzing the shear stress–slip displacement curves recorded by the testing machine (Figure 6), the micro-mechanism by which CNTs content variation controls the interfacial failure mode was clearly revealed. Figure 6 shows that the shear stress–slip curves of representative specimens exhibit distinctly different morphological evolution patterns, reflecting the fundamental transition of the material from brittle to pseudo-ductile behavior.

(1) Typical Brittle Fracture Stage (0.10% Graphene + 0% CNTs): As shown in Figure 6(a), the curve of Group C0 (0.10% graphene alone) exhibits extremely typical brittle failure characteristics. In the initial loading stage, the interfacial shear stress increased linearly with slip displacement, with almost no pre-peak yield stage. Once the ultimate bond strength of 2.11 MPa was reached, the curve dropped vertically in a cliff-like manner, and the stress instantly fell to zero. This indicates that in the absence of one-dimensional fiber bridging, once an interface crack initiated, it rapidly propagated through the entire cross-section, resulting in instantaneous debonding slip. The area under the curve (fracture energy) was extremely small, reflecting the weak ability of the interface to resist dynamic impact and deformation.

(2) Pseudo-Ductile Transition Stage (0.10% Graphene + 0.04% CNTs): As shown in Figure 6(b), with the introduction of an appropriate amount of CNTs, the interfacial failure mode underwent a significant change. For Groups C2/C3, not only did the peak strength increase dramatically to 5.88 MPa, but more importantly, the curve morphology changed: some nonlinear bending (pre-peak yield) appeared before reaching the peak; after exceeding the peak, the stress did not disappear instantaneously but exhibited a relatively gentle descending segment, retaining significant residual friction at the end of displacement. This macroscopic mechanical phenomenon preliminarily confirms

the toughening effect of CNTs as “micro-rebars”, and the interfacial failure transitions from brittle fracture to pseudo-ductile failure.

(3) Synergistic Toughening and Pull-Out Energy Dissipation Stage (0.10% Graphene + 0.10% CNTs): When the CNTs content reached the optimal proportion (0.10%), Figure 6(c) presents the excellent fracture toughness of this composite system, which is also a core innovation of this study. This curve not only achieves the highest peak strength (6.06 MPa) but also exhibits unique “stepwise” or “serrated” rebound and descending characteristics after the peak. This significant staged stress fluctuation is the most intuitive manifestation of CNTs playing “bridging anchoring” and “pull-out” effects in the ITZ. During interfacial slip, the numerous CNTs spanning the cracks were continuously tensioned, underwent elastic deformation, and ultimately were pulled out or broken from the cement matrix. Each serrated rebound represents the dissipation of a large amount of fracture energy by a batch of CNTs through interfacial friction, thereby effectively delaying the propagation of the main crack and maintaining a high residual bond strength after failure. The area under this curve is maximized, indicating that the system achieves the ultimate synergistic interfacial toughening.

(4) Agglomeration Softening and Defect Stage (0.10% Graphene + 0.12% CNTs): However, when the CNTs content was excessive (0.12%, Figure 6(d)), the initial tangent slope of the curve decreased significantly, the peak became very blunt and rounded, and the curve exhibited smooth, continuous softening failure characteristics. This confirms the previously described nano-agglomeration effect: excessive CNTs become entangled and agglomerated at the interface, forming weak macro-scale defects. These defective areas cannot effectively transmit stress or exert fiber reinforcement, leading to local slip and plastic yield at lower stresses. Macroscopically, this manifests as a reduction in peak strength and the disappearance of bridging energy dissipation features.

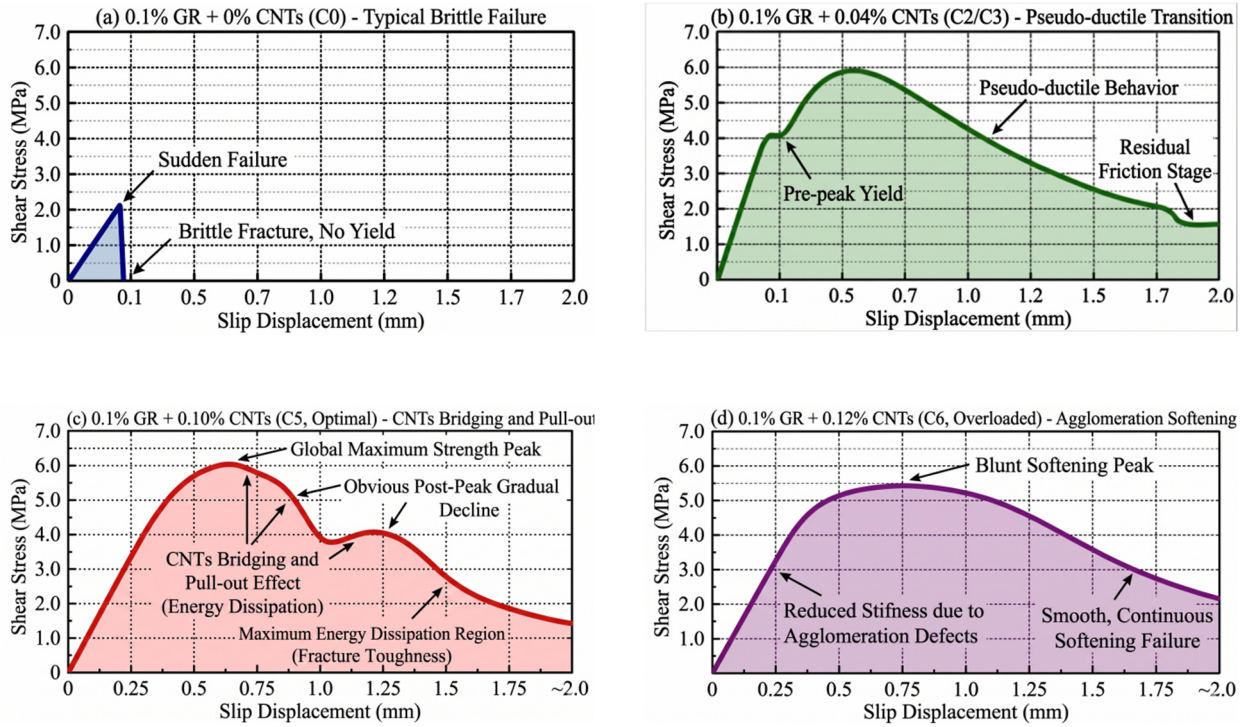


Figure 6. Shear stress-slip displacement curves of the second interface

The morphological evolution of the shear stress–slip curves strongly demonstrates that the combination of graphene and an appropriate amount of CNTs not only improves the absolute shear

resistance of the geothermal well cementing interface but also endows the second interface with high fracture toughness and residual load-bearing capacity by constructing a cross-scale “line-surface” crack-arresting network, providing long-term protection against interface debonding induced by thermal cycling.

4. MICRO-REINFORCEMENT MECHANISM OF SECOND-INTERFACE BONDING

4.1. ITZ Morphology Evolution and Densification Mechanism

To reveal the nature of the changes in macroscopic mechanical bond strength at the second interface from the microscale, this section first compares and analyzes the morphology evolution and hydration product distribution characteristics in the ITZ of the plain cement baseline group (B0) and the group with 0.10% graphene alone (C0).

Figure 7 shows the second-interface morphology and EDS spectra of the B0 group specimens after push-out failure. At a low magnification of 100 μm (Figure 7a), the unmodified ITZ can be clearly observed to have an extremely loose structure, with numerous wide, connected microcracks within the matrix. This high porosity and macro-scale fissures are natural defects that lead to fluid channeling and stress concentration. At a higher magnification of 10 μm (Figure 7b), it can be seen that the surroundings of the microcracks are mainly occupied by massive C-S-H gel and coarse portlandite (CH) crystals, with very loose stacking between the products and a lack of effective spatial cross-linking. The EDS spot analysis (Figure 7c) shows a relatively high calcium content of 53.2% and very little silicon, confirming that this micro-zone is a typical highly alkaline, low-strength CH-rich area. In geothermal cementing, the significant directional enrichment of such coarse, cleavage-plane-rich CH crystals at the interface greatly weakens the physical mechanical interlocking between the cement stone and the rock, microscopically explaining the extremely low macroscopic bond strength (only 0.41 MPa) and instantaneous brittle fracture observed for Group B0.

With the introduction of 0.10% graphene, a fundamental densification transformation occurred in the second-interface microstructure. Figure 8 presents the interfacial microstructure of the C0 group. From the overall view at 200 μm (Figure 8a), the number of large cracks was significantly reduced, the overall density of the cement matrix was greatly improved, and the matrix exhibited a more homogeneous platy structure. At a high magnification of 20 μm (Figure 8b), the C-S-H gel, needle-like ettringite (AFt), and graphene sheets can be seen to be tightly interwoven. EDS spot analysis of the flake-like attachments (Figure 8c) detected a carbon content of 43.3%, explicitly confirming the widespread presence of two-dimensional graphene nanoplatelets at the interface. Simultaneously, the presence of certain proportions of Ca and Si elements indicates that hydration products directly crystallized and attached to the graphene surfaces.

This significant densification phenomenon strongly confirms the “template nucleation effect” and “interface optimization” mechanism of graphene. By virtue of its large specific surface area, two-dimensional graphene acts as an excellent nucleation substrate at the second interface, not only lowering the nucleation barrier for hydration products but also guiding the oriented, dense growth of secondary C-S-H gel on its surface and in the surrounding nanopores. This synergistic effect of physical filling and nucleation promotion greatly consumes the brittle CH phase at the interface, fills the originally wide micro-annuli, and improves the close contact between the cement stone and the sandstone surface. The microstructural crack closure and densification perfectly correspond to the macroscopic bond strength jump from 0.41 MPa to 2.11 MPa.

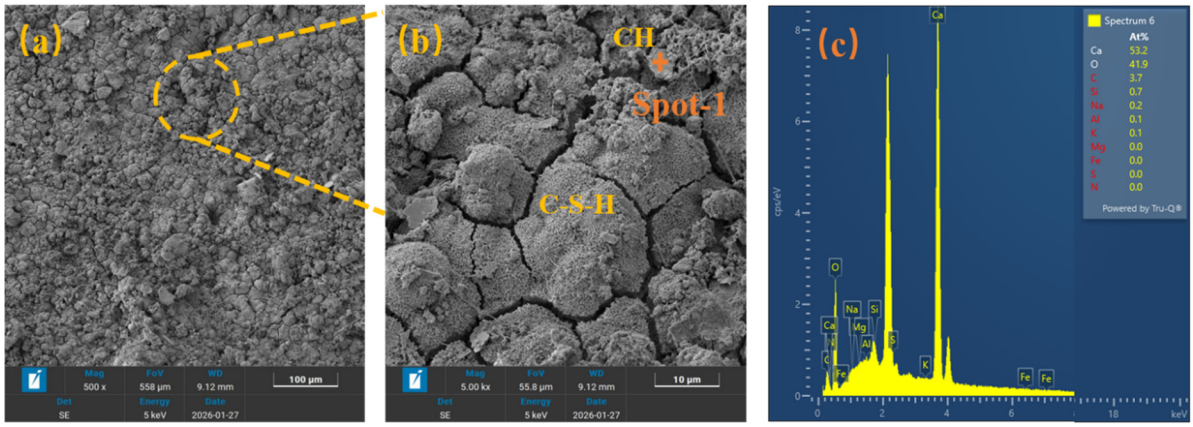


Figure 7. SEM images and EDS spectra of the second interface of Group B0 (b is an enlarged view of a)

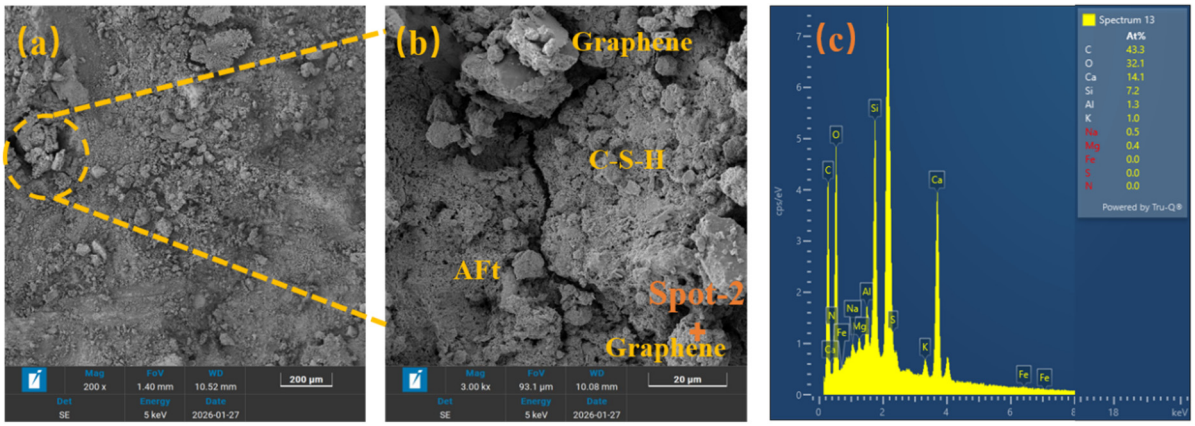


Figure 8. SEM images and EDS spectra of the second interface of Group C0 (b is an enlarged view of a)

4.2. Interfacial Element Migration Law and Chemical Bonding Characteristics

The bond strength of the second interface depends not only on the physical "bridging" and "mechanical interlocking" provided by CNTs and graphene but also on the chemical element migration and secondary hydration reactions between the rock and cement stone. To explore the in-depth influence of hybrid nanomaterials on interfacial chemical bonding, EDS mapping was used to quantitatively analyze the elemental distribution characteristics of the bonding interface under different mix proportions. Figures 9 and 10 quantitatively reveal the micro-element evolution and chemical bonding characteristics of the ITZ under different CNTs network configurations. The sandstone core is mainly composed of quartz and feldspar minerals, rich in Si, Al, and O, while the cement stone side is rich in Ca, Si, and O (calcium silicate hydrate and CH). Therefore, the migration depth of Ca toward the rock surface and the Ca/Si ratio at the interface are key indicators for assessing the quality of interfacial chemical bonding.

A comparison of the two sets of EDS data reveals that the interfacial chemical composition changed significantly after optimization of the CNTs network. Under the non-optimal network state (Figure 9), the interface micro-zone exhibited an atomic percentage of Ca of 8.68% and of Si of 14.73%, giving a local Ca/Si ratio of approximately 0.59. This relatively high calcium proportion indicates that despite some physical connection provided by the nanomaterials, a considerable amount of free calcium ions remained enriched at the interface, tending to crystallize into brittle CH crystals with pronounced cleavage planes, which limited further improvement of the interface strength.

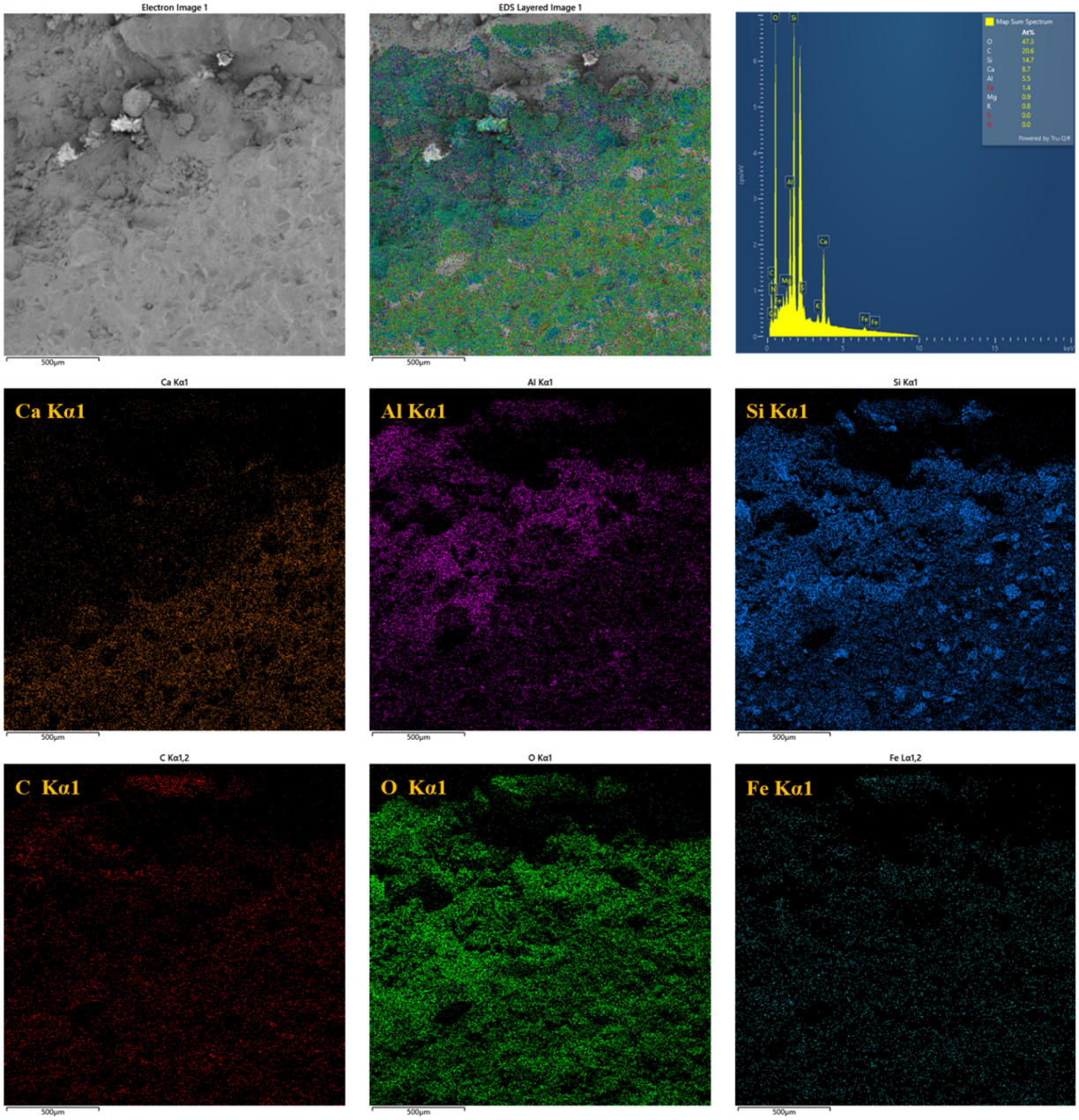


Figure 9. EDS mapping and elemental quantification of the ITZ of Group C1

In contrast, for Group C5, which achieved the optimal "line-surface" synergistic network (Figure 10), the elemental distribution characteristics at the interface underwent a qualitative change. EDS results showed that the atomic percentage of Ca in the ITZ decreased significantly to 6.89%, while the relative abundances of Si and Al leached from the rock side increased to 15.93% and 6.78%, respectively, resulting in a sharp reduction of the interfacial Ca/Si atomic ratio to 0.43. This transformation in micro-chemical characteristics has high mechanical significance. On one hand, the lower Ca/Si ratio confirms that the three-dimensional network composed of graphene and CNTs effectively trapped and dispersed moisture, greatly promoting the deep pozzolanic reaction between silica fume and the CH generated by cement hydration. On the other hand, the resulting low-Ca/Si C-S-H gel attached directly to the silica-rich sandstone surface, achieving a transition from weak physical van der Waals forces to strong chemical bonding (Si-O-Si or Si-O-Ca bonds).

The combination of graphene with an appropriate amount of CNTs not only physically spanned microcracks at the macroscopic level but also chemically optimized the elemental concentration

gradient in the ITZ. By substantially consuming the brittle, Ca-rich CH phase in the interface-sensitive zone and promoting the networked growth of dense silicate gel, the nanocomposite system achieves dual reinforcement of "physical anchoring" and "chemical bonding". This provides decisive chemical thermodynamic evidence for the excellent shear strength of up to 6.06 MPa observed for Group C5 in macroscopic testing.

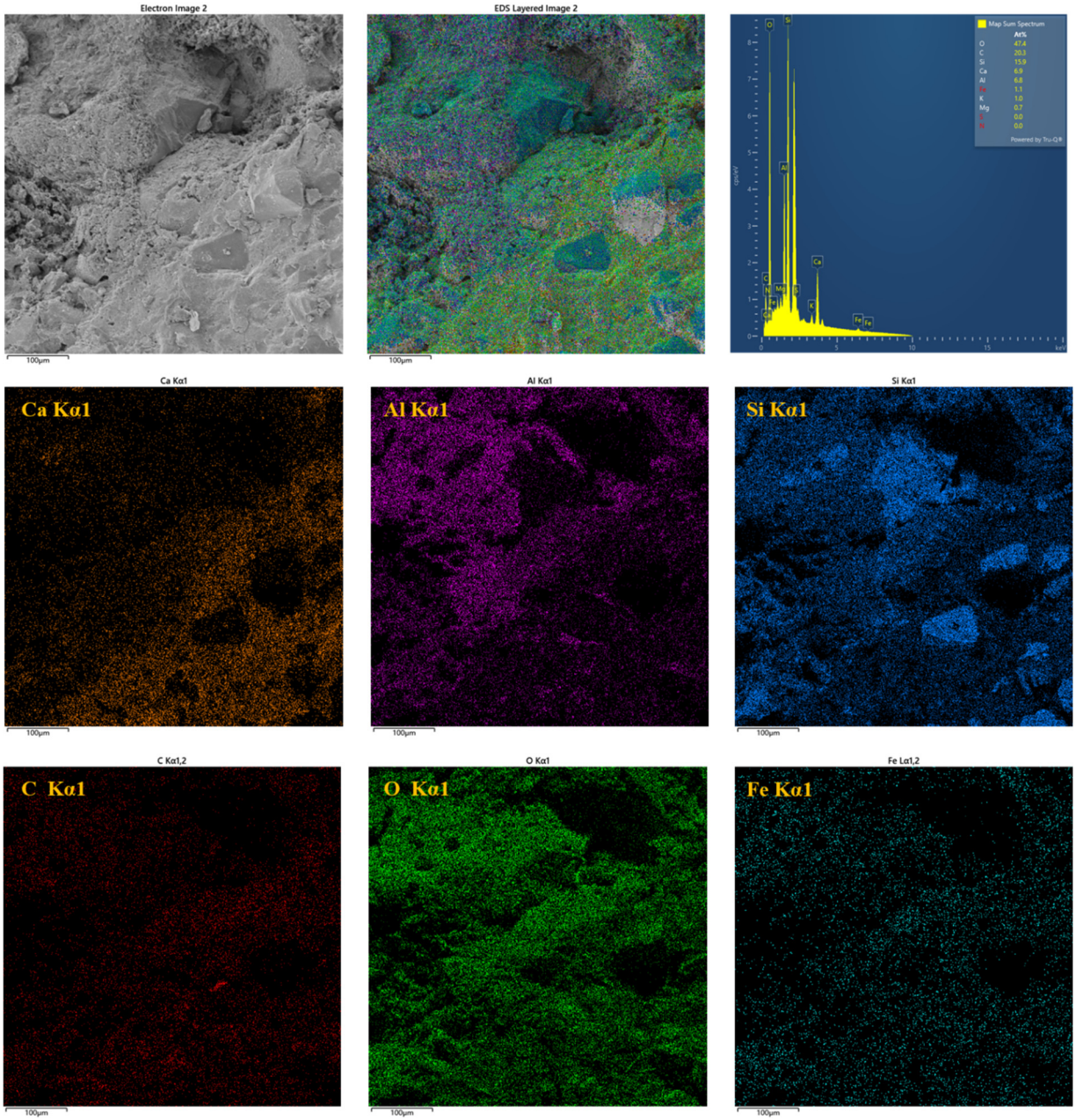


Figure 10. EDS mapping and elemental quantification of the ITZ of Group C5

5. EVALUATION OF SECOND-INTERFACE BONDING QUALITY

For the complex thermal-mechanical alternating conditions of geothermal wells in the Ordos Basin, a single strength indicator is insufficient to fully reflect the actual service state of the second interface. Therefore, systematically evaluates the comprehensive second-interface bonding quality of the nanocomposite system based on four dimensions: shear strength, deformation toughness, interfacial density, and chemical bonding quality.

From the perspective of mechanical properties, the conventional plain cement (B0) exhibited extremely low interfacial shear strength (only 0.41 MPa) and showed typical instantaneous brittle fracture upon failure. Such an interface is highly susceptible to debonding and peeling when subjected to the frequent thermal expansion and contraction shocks of geothermal wells. In contrast, for the hybrid system with both graphene and CNTs at 0.10%, the ultimate interfacial bond strength was significantly increased to 6.06 MPa. More importantly, the "bridging" and "pull-out" energy dissipation mechanisms of CNTs endowed the interface with excellent ductility and fracture toughness. This synergistic strengthening and toughening can effectively alleviate the interfacial stress concentration induced by temperature fluctuations, thereby enhancing the fatigue resistance of the wellbore during long-term service.

From the perspective of microstructure and chemical bonding, the unmodified ITZ typically exhibits obvious micro-annuli and loosely packed hydration products. The introduction of an appropriate amount of graphene and CNTs constructs a dense three-dimensional interpenetrating network at the interface, physically filling micro-pores and limiting matrix shrinkage deformation. Meanwhile, quantitative EDS mapping results show that the formation of the optimal hybrid network significantly reduced the Ca/Si atomic ratio in the interface micro-zone from 0.59 to 0.43. This indicates that a large amount of brittle, cleavage-plane-prone CH phase at the interface was effectively consumed and transformed into high-strength C-S-H gel. This dense gel attaches to the sandstone core surface, gradually transforming the interface from weak physical van der Waals adhesion to tightly connected chemical bonding, fundamentally blocking the pathways for fluid channeling.

To visually compare the interfacial service potential of different systems, a radar chart for comprehensive second-interface bonding quality evaluation was drawn (Figure 11). It can be seen that the optimal hybrid group (C5) achieved comprehensive superiority over the baseline group in all four dimensions: shear strength, fracture toughness, density, and chemical bonding. Combined with the bulk property test results from Chapter 3, the hybrid proportion of 0.10% graphene and 0.10% CNTs not only achieved simultaneous improvements in thermal conductivity and compressive strength but also endowed the second interface with extremely high comprehensive bonding quality, providing a reliable material foundation for solving the "poor thermal conduction" and "weak interface" problems in geothermal well cementing engineering.

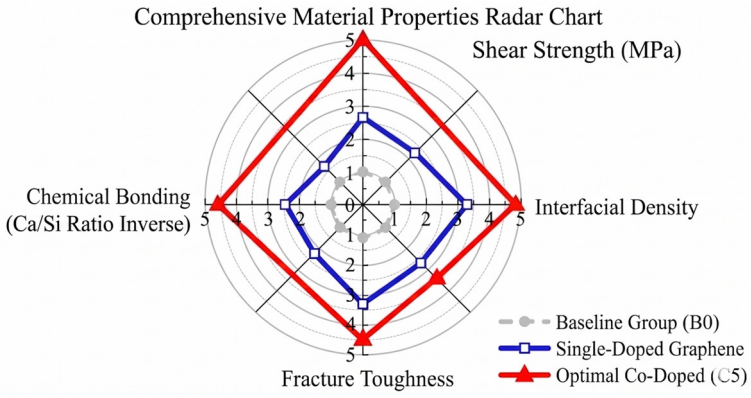


Figure 11. Radar chart for comprehensive second-interface bonding quality evaluation

6. CONCLUSION

(1) The synergistic incorporation of graphene and carbon nanotubes (CNTs) significantly improved the second-interface bond strength and fracture toughness of the cement sheath. The "line-surface" three-dimensional interpenetrating network constructed by the two nanomaterials elevated the interfacial shear resistance from an extremely low level to several times higher, exhibiting a

pronounced long-term strengthening characteristic. As the CNTs content increased, the interfacial bond strength followed a non-linear evolution pattern of “rapid increase—saturation—agglomeration-induced decay”. With the addition of an appropriate amount of CNTs, the interfacial failure mode transitioned from brittle “cliff-like” instantaneous debonding to pseudo-ductile failure characterized by serrated rebounds, which was attributed to the “bridging–pull-out” energy dissipation mechanism of CNTs spanning microcracks. Microstructural observations confirmed that graphene acted as a template nucleation site, guiding the oriented and dense growth of hydration products, while CNTs interspersed between the sheets and filled micron-scale pores, effectively inhibiting microcrack propagation. However, excessive CNTs led to severe agglomeration, transforming into low-strength defects and causing interfacial degradation.

(2) The hybrid nanomaterial network fundamentally optimized the element migration and bonding characteristics of the interfacial transition zone. The secondary pozzolanic reaction at the interface was significantly stimulated. A large amount of the brittle Ca-rich phase was consumed and transformed into low-Ca/Si C-S-H gel, leading to a substantial reduction in the interfacial Ca/Si atomic ratio. The interface bonding evolved from physical van der Waals forces to chemical covalent bonding (Si–O–Si/Si–O–Ca), achieving dual reinforcement of “physical anchoring” and “chemical bonding”. In summary, the synergistic combination of graphene and CNTs demonstrated significant synergy in enhancing mechanical properties, improving fracture toughness, and optimizing chemical bonding. This study provides a clear theoretical basis and experimental support for the integrated material design of “high thermal conductivity and strong interface” in geothermal well cementing engineering.

REFERENCES

[1] Li S, Wang D, Wang Z, et al. Strategic status and role of deep underground space development and utilization in advancing new energy[J]. Acta Petrolei Sinica, 2026, 47(1): 241.

[2] XIONG Y, ZHANG P, LU H, et al. Evaluation and research progress of CO 2 sequestration in deep coal seams[J]. Coal geology & exploration, 54(4): 76-94.

[3] Shujie L I U, Yi H, Haodong C, et al. Innovation and Practice of Key Technologies for Drilling and Completion in Deepwater High-Pressure Gas Field of “Deep Sea No. 1” Phase II Project[J]. Petroleum Drilling Techniques, 2025, 53(3): 20-29.

[4] Hou D, Zhang Z, Geng Y, et al. Experimental study on the channeling leakage properties of compact-size casing-cement sheath-stratum assembly in deep and ultra-deep wells[J]. Process Safety and Environmental Protection, 2023, 178: 881-892.

[5] Tian H, Liu H, Bu Y, et al. Effect of composite interface enhancer on the cementation strength of shale formation–cement ring interface[J]. Processes, 2024, 12(2): 405..

[6] Wang L, Liu B, Guo Y, et al. Experimental investigation of the cementation and tensile properties of cement to formation interface considering surface irregularity and drilling mud residue[J]. Journal of Petroleum Exploration and Production Technology, 2023, 13(2): 705-721.

[7] Zhang X, Jia C, Yao J, et al. An evaluation framework for production performance of high-temperature fractured and karstified geothermal reservoirs: Production mechanism, sensitivity study, and key parameters ranking[J]. Gondwana Research, 2023, 122: 279-305.

[8] Qiao M, Zhou Y, Jing Z, et al. Heat extraction analysis of an innovative single-well open-loop geothermal system using scCO2[J]. Energy, 2025, 328: 136502.

[9] Su D, Huang S, Li Z, et al. Sealing Integrity Evaluation and Optimization of Cement Sheath-Formation Interface under Different Formation Conditions during Fracturing[J]. Journal of Earth Science, 2025, 36(1): 223-232.

[10] Yan Y, Guan Z, Yan W. Modeling of micro-annulus propagation along cementing interface in stimulated horizontal wellbore[J]. Geosystem Engineering, 2021, 24(5-6): 247-255.

[11] Shengli C, Wang L, Zhu D, et al. Experimental study and thoughts on safety and environmental protection of steam flooding of horizontal wells in a heavy oil reservoir[J]. ACS omega, 2022, 7(18): 15488-15498..

[12] Bageri B S, Gamal H, Elkatatny S, et al. Effect of different weighting agents on drilling fluids and filter cake properties in sandstone formations[J]. ACS omega, 2021, 6(24): 16176-16186.

[13] Rahmati M, Khosravi M, Tanha A A, et al. Evaluation of formation damage and filter cake removal with a new LPM drilling fluid additive[J]. Results in Engineering, 2024, 23: 102656.

[14] Hu H, Hu Y, Weng X. Study on Filter Cake Removal Fluid of EZFLOW Weak Gel Drilling Fluid[J]. Gels, 2025, 11(5): 347.

[15] Adebayo A R, Bageri B S. A simple NMR methodology for evaluating filter cake properties and drilling fluid-induced formation damage[J]. Journal of Petroleum Exploration and Production Technology, 2020, 10(4): 1643-1655.

[16] Zhang D, Zhan Z. Experimental investigation of interfaces in graphene materials/copper composites from a new perspective[J]. Rsc Advances, 2016, 6(57): 52219-52226.

[17] Deb D, Mishra P C, Singh S. Effect of SiC Nanoparticles on the Microstructural and Physico-Mechanical Properties of Agro-Bio-Wastes (RHA–ESA) Reinforced T6 Heat Treated Al Hybrid Nanocomposite[J]. Silicon, 2025, 17(11): 2581-2603..

[18] Dallaston M C, Jackson M J W, Morrow L C, et al. Two-interface and thin-filament approximation in Hele-Shaw channel flow[J]. Journal of Fluid Mechanics, 2024, 988: A31.

[19] Zhao Z, Li M, Zhang Z, et al. Experimental study on the factors affecting cement bond strength at the second interface of oil-gas well[J]. Journal of Dispersion Science and Technology, 2026, 47(4): 649-659.

[20] Dutka B, Nurkowski J, Tram M, et al. Comparison of the Water Absorbability of Rocks and Composite-Cement Stones for Optimal Characterization of Sustainable Building Materials[J]. Sustainability, 2025, 18(1): 198.